PHYSICAL REVIEW A **87**, 053403 (2013)

Theoretical study of high-order-harmonic generation from asymmetric diatomic molecules

Xiang-Yang Miao[*] and Hui-Ni Du

College of Physics and Information Engineering, Shanxi Normal University, Linfen 041004, People's Republic of China

(Received 28 December 2012; revised manuscript received 4 April 2013; published 6 May 2013)

The molecular high-order-harmonic generation (molecular HHG) of HeH^{2+} is investigated by numerical integration of the non-Born-Oppenheimer time-dependent Schrödinger equation. The results show that multichannel interference plays a very important role in the process of asymmetric molecular high-order-harmonic generation. By means of the classical returning kinetic energy map and the time-frequency distribution, the mechanism of molecular HHG for HeH^{2+} is discussed in detail. Further studies show that asymmetric molecular harmonic emission is very sensitive to the nuclear signatures, i.e., the initial vibrational state and the isotopic effect. Besides, the electron-nuclear probability density distributions are calculated to better understand the process of the asymmetric molecular HHG, from which the electron-nuclear dynamics can be revealed.

DOI: 10.1103/PhysRevA.87.053403 PACS number(s): 33.80.Rv, 42.65.Re, 42.25.Hz

I. INTRODUCTION

The interaction between intense laser pulses and atoms [1,2] or molecules [3] has received considerable attention recently. Many phenomena, such as bond softening and bond hardening [4–6], high-order-harmonic generation (HHG) [7,8], above-threshold dissociation and ionization [9], and above-threshold Coulomb explosion (CE) [10,11], have been discovered. Because the HHG can provide a type of coherence light source of extremely short wavelength, it can be widely used in many fields such as attosecond pulse generation [12,13], plasma spectroscopy [14], and x-ray fluorescence analysis [15]. It is well known that a typical HHG spectrum presents a rapid decay of the lower-order harmonics, a long plateau of almost constant conversion efficiency, as well as a short cutoff with photon energy around $I_p + 3.17U_p$ (I_p is the ionization potential and $U_p = I/4\omega^2$ denotes the ponderomotive energy). In order to interpret the HHG mechanism, a semiclassical three-step model, which is able to explain above-threshold HHG [16,17] but not to clarify the short trajectories in the below-threshold regime, is adopted extensively [18,19]. That is to say, the electrons tunnel through the barrier and then accelerate in the laser field; finally, when the laser field reverses its direction, the electron may return and recombine with the parent ion, and emit a harmonic photon simultaneously.

When symmetric two-center molecules are considered, in addition to recolliding with the parent nucleus, electrons recolliding with the neighboring nucleus can also occur due to the larger number of molecular degrees of freedom. Thus, the dynamics of the HHG of the molecular systems are different from the atom systems, strongly depending on the nuclear motion and the molecular structures. For instance, Zuo *et al.* [20] and Moreno *et al.* [21] find that, at higher initial excited vibrational state, both the harmonic intensity and the harmonic cutoff energy from the $H_2{}^+$ ion are enhanced. Furthermore, Lein [22] theoretically demonstrates that the harmonic spectra generated from the molecules would be approximately relevant to the nuclei vibrational autocorrelation function. Based on that theoretical work, Baker *et al.* [23] have done high-precision experiments and probed the ultrafast motions of the nuclei in diatomic molecules. More recently, Guo *et al.* [24] and Feng and Chu [25] demonstrate that the harmonic emissions from the $H_2{}^+$ and $D_2{}^+$ ions are very sensitive to the nuclear motion, with more intense harmonics generated in the lighter isotopes.

For asymmetric molecular ions, such as HeH^{2+}, LiH^{3+}, and BeH^{4+}, which have permanent dipoles and multiple centers, the charge is mainly localized on the heavier nucleus as the electronic wave function mainly concentrates on the heavier ion. As the simplest asymmetric molecule, the cation of HeH has been the subject of many works on laser-induced phenomena, such as high-order-harmonic generation [26,27], enhanced ionization [28], double ionization [29], and photodissociation [30]. For instance, Lan *et al.* [31] present a new method for isolated attosecond pulse generation from high harmonics in the plateau with asymmetric molecules. Additionally, Bian and Bandrauk [32–34] investigate the asymmetric diatomic molecular high-order-harmonic generation (molecular HHG), in which the interference of the different quantum paths can be found in the HHG of HeH^{2+} molecular ion. Most recently, based on the quantum orbital theory, Chen and Zhang [35] investigate the emission times of HHG from asymmetric molecule HeH^{2+}, from which the electron dynamics in laser-excited asymmetric molecule can be traced.

Most of the previous theoretical studies [31–34] for the asymmetric molecules have invoked the Born-Oppenheimer (BO) separation of the electronic and nuclear degrees of freedom. However, the non-Born-Oppenheimer (NBO) simulations of molecular HHG in the H_2, $H_2{}^+$ systems show that the nuclear motion can influence molecular high-order-harmonic generation, such as rapid enhancement of the ionization, fast movement of nuclei, and dispersion nuclear wave packets [36,37]. Electrons respond essentially instantaneously on the time scale of either the nuclear motion or the optical period of the laser field, whereas, as laser pulses become shorter and more intense, the electronic structure of the molecule becomes distorted, differing substantially from its field-free BO state [36,38]. Therefore, under the influence of intense laser field, any predictions based on the BO approximation will be inaccurate because of considerable extending of the nuclear packet in a short time. In the present work, by solving the NBO approximation time-dependent Schrödinger equation (TDSE), we not only present the multichannel interference in

---

[*] sxxymiao@126.com

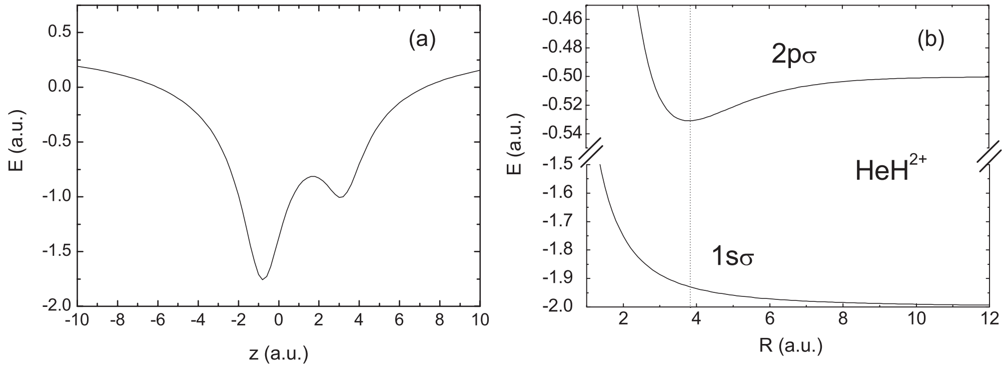

FIG. 1. (a) Coulomb potential for asymmetric molecules of HeH^{2+} when the internuclear distance is 3.9 a.u. (b) Potential energy curves for the lowest two states of HeH^{2+}.

the process of molecular HHG for the asymmetric diatomic molecule, but the effects of the nuclear signature, i.e., the initial vibration state and the isotopic effect on the molecular HHG are also studied in detail.

The paper is organized as follows. We briefly introduce the theoretical model and numerical method in Sec. II. The results and discussions are presented in Sec. III. The conclusion of our paper is in Sec. IV.

II. NUMERICAL METHOD AND THEORETICAL MODEL

In our calculations, the molecular HHG can be investigated by solving the $1+1$ dimensional $(1+1\text{D})$ time-dependent Schrödinger equation (TDSE) via the parallel quantum wave-packet computer code LZH-DICP [39,40]. In this model, we consider the HeH^{2+} (HeD^{2+}) molecule ion as a three-particle system, which consists of the He nucleus, the H (D) nucleus, and an electron. In a linearly polarized laser field, the molecules can be partially aligned along the polarization direction due to the evolution of the excited rotational wave packet. For simplification, the nuclear and the electronic motion are restricted to the laser polarization direction. In the dipole approximation and the length gauge, the TDSE is given by [in atomic units (a.u.) $e = \hbar = m_e = 1$, which are used throughout unless otherwise indicated]

$$i\frac{\partial}{\partial t}\psi(R,z,t) = [H_0 + V(t)]\psi(R,z,t), \tag{1}$$

where $H_0 = T_n + T_e + V_0$ is the field-free Hamiltonian with

$$T_n = -\frac{1}{2\mu}\frac{\partial^2}{\partial R^2},$$
$$T_e = -\frac{1}{2\mu_e}\frac{\partial^2}{\partial z^2},$$
$$V_0 = \frac{C_H C_{He}}{R} - \frac{C_H}{\sqrt{(z - z_H)^2 + \alpha}} - \frac{C_{He}}{\sqrt{(z - z_{He})^2 + \alpha}},$$

and $V(t)$ is the electron potential including the laser-molecule interaction. Here, R is the internuclear distance, C_H and C_{He} are the electron charges of the nuclei, and $z_H = m_{He}/(m_H + m_{He})R$ and $z_{He} = -m_H/(m_H + m_{He})R$ are the positions of H and He, respectively. $\mu = (1/m_H + 1/m_{He})^{-1}$ and $\mu_e = (m_H + m_{He})/(m_H + m_{He} + 1)$ are the reduced masses, with m_H and m_{He} the masses of H and He. The soft-core parameter $a = 1$ has been chosen so that the model of HeH^{2+} yields the $2p\sigma$ bound state energy and equilibrium distance of -0.5317 and 3.9 a.u. [30], respectively. In Fig. 1(a), we present the Coulomb potential for the asymmetric molecule, which shows a double-well structure. The electron prefers localizing at the deeper well, -1 a.u., indicating a permanent molecular dipole. The interaction with the laser is treated in the dipole approximation and length gauge,

$$V(t) = \left[\frac{C_{He}m_H - C_H m_{He}}{m_H + m_{He}}R + \left(1 + \frac{C_H + -1}{m_H + m_{He} + 1}\right)z\right]E(t). \tag{2}$$

A linearly polarized laser pulse is adopted as the driving laser. The laser electric field is given by

$$E(t) = E_0 f(t)\cos(\omega t), \tag{3}$$

where E_0 and ω are the peak amplitude and the frequency of the fundamental laser pulses, respectively. The pulse envelope $f(t)$ is a five-optical-cycle trapezoidal pulse with one cycle ramp on, three cycles constant, and one cycle ramp off. The atomic unit is used and one optical cycle (o.c.) is 5.33 fs (the period of a 1600-nm laser pulse) throughout this paper unless stated otherwise.

Before the time evolution of the wave function, an initial state is requisite. However, a stable wave function cannot be obtained directly by imaging time propagation of Eq. (1) because the energy of the $1s\sigma$ state shown in Fig. 1(b) decreases monotonously with increasing the internuclear distance; thus the lowest state $1s\sigma$ is unstable. This can be understood as that the vibrational wave packets are not bounded by the $1s\sigma$ curve. In our calculation, the first excited state, $2p\sigma$, which is the lowest electronic bound state of HeH^{2+}, is chosen to be the initial state of the system. As shown in Fig. 1(b), the $2p\sigma$ state shows a minimum at $R = 3.9$ a.u., indicating a stable state with its equilibrium distance at about 3.9 a.u. All these features are in agreement with the potential of HeH^{2+} reported in Ref. [30], indicating the effectiveness of our model.

The time-dependent wave function is advanced using the standard second-order split-operator method [41],

$$\psi(R,z;t+\delta t) = e^{-iT\delta t/2}e^{-iV\delta t}e^{-iT\delta t/2}\psi(R,z;t) + O(\delta t^3), \tag{4}$$

where T is the kinetic energy operator, and V is the interaction potential taking all the potential energy of the system plus a purely imaginary term to produce an absorbing boundary.

In the TDSE calculations, the wave function is discrete on a two-dimensional grid spanned by $-100 \leqslant z \leqslant 100$ containing 1000 grid points and $0 \leqslant R \leqslant 30$ containing 300 grid points. The time step of wave function propagation, which is associated with the nuclear motion, is set to be 0.1. In order to avoid spurious reflections of the wave function from the boundary $z = \pm 100$ and $R = 30$, the wave function is multiplied by a $\cos 1/8$ mask function over a range of $|z| = 80 - 100$, and $R = 25–30$ per evolving step.

According to the Ehrenfest theorem [42], the time-dependent dipole acceleration can be written as

$$\begin{aligned} d_A(t) &= \langle \psi(R,z,t)| - \frac{\partial V(z,t)}{\partial z} |\psi(R,z,t)\rangle \\ &= \langle \psi(R,z,t)| - \frac{\partial V_C}{\partial z} \\ &\quad + \left(1 + \frac{C_{\mathrm{H}} + C_{\mathrm{He}} - 1}{m_{\mathrm{H}} + m_{\mathrm{He}} + 1}\right) E(t)\,|\psi(R,z,t)\rangle\,. \end{aligned} \tag{5}$$

The harmonic spectra are obtained by Fourier transforming the time-dependent dipole acceleration:

$$P_A(\omega) = \left| \frac{1}{\sqrt{2\pi}} \int d_A(t) e^{-i\omega t} dt \right|^2 . \tag{6}$$

The time-dependent ionization probability is calculated by

$$P(t) = \int_0^t dt' \int_0^{R_s} dR j(R,z,t'), \tag{7}$$

where $j = \frac{1}{\mu_e} \mathrm{Im}[\phi^* \delta(z - z_0) \frac{\partial}{\partial z} \phi]$.

To study the detailed spectral and temporal structures of HHG, we perform the time-frequency analysis by means of the wavelet transform [43]

$$d_\omega(t) = \int d_A(t') \sqrt{\omega} W\left[\omega(t' - t)\right] dt'. \tag{8}$$

The mother wavelet we use is a Morlet wavelet [44]:

$$W(x) = \frac{1}{\sqrt{\tau}} e^{ix} \exp\left(\frac{-x^2}{2\tau^2}\right). \tag{9}$$

In the classical calculations, the electron kinetic energy can be calculated by integrating the classical equation of motion with the initial condition of the electron being at rest immediately after ionization that occurs at time t'. The classical velocity v of the electron at the time of recombination with the nucleus t_r is $v = -\int_{t'}^{t_r} E(t) dt$. The electron displacement x_d can be written as $x_d = \int_{t'}^{t_r} v dt$. A recollision between the ionized electron and its parent ion (i.e., the homonuclear recombination) or its neighboring ion (i.e., the heteronuclear recombination) occurs whenever $x_d(t_r) = 0$ or $x_d(t_r) = \pm R$. The kinetic energy E_{kin} of the returning electrons is $E_{\mathrm{kin}} = \frac{1}{2} v^2$, and the harmonic generation order N is given by $N\omega = I_p + E_{\mathrm{kin}}$, where I_p is the ionization potential.

III. RESULTS AND DISCUSSION

Just as the description mentioned above, the previous studies of the asymmetric molecular harmonic generation have been mainly based on the BO approximation which ignores the couplings of the electronic and nuclear wave packet [31–34]; however, the high correlation of nuclear motion and intense infrared laser field have been revealed in some experimental and theoretical works on tunnel ionization of the molecular systems [45,46]. Using intense laser pulses to explore the couplings of the electrons and nuclei in the molecular HHG [36,37,47] has drawn a great deal of attention. In this section, the high-order-harmonic generation in asymmetric molecular ion will be more deeply investigated by taking the couplings of the electronic and nuclear wave packet into account.

A. The multichannel interference in the process of molecular HHG

In consideration of the inherent characteristic of the HeH^{2+} molecular ion, in Fig. 2, the schematic illustration of the electron motion for the HeH^{2+} molecular ion is presented. The black solid and dotted lines present the complex energy combined Coulomb and laser field potential for polarization direction of the laser pulse parallel (black solid line) or antiparallel (black dotted line) to the molecular axis. The red and black circles represent the electrons in the process of ionization and recombination, respectively. The amplitude $|F|$ corresponds to the peak laser intensity and the direction presents the polarization direction of the laser pulse. On the one hand, when the laser field is parallel to the molecular axis, some of the electrons ionize from the He atom, and then accelerate in the laser field; finally, when the laser field reverses its direction, the electrons may return back and recombine with He^{2+} ($\mathrm{He} \rightarrow e \rightarrow \mathrm{He}$) or H^+ ($\mathrm{He} \rightarrow e \rightarrow \mathrm{H}$) ion, and emit harmonic photons. Furthermore, due to the permanent dipole in the HeH^{2+}, the probability of the recombination process is lower for H^+, compared with the electron recombining with He^{2+}. Therefore, the probability of $\mathrm{He} \rightarrow e \rightarrow \mathrm{He}$ process is

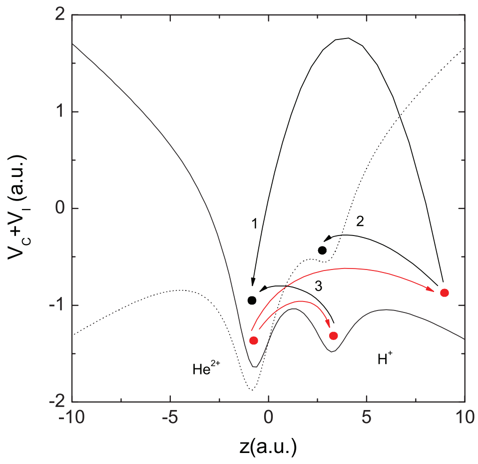

FIG. 2. (Color online) Schematic of the electron motion in HeH^{2+}. The black solid (dotted) line shows the combined Coulomb and electron field potential for polarization direction of the laser pulse parallel (black solid line) or antiparallel (black dotted line) to the molecular axis, respectively.

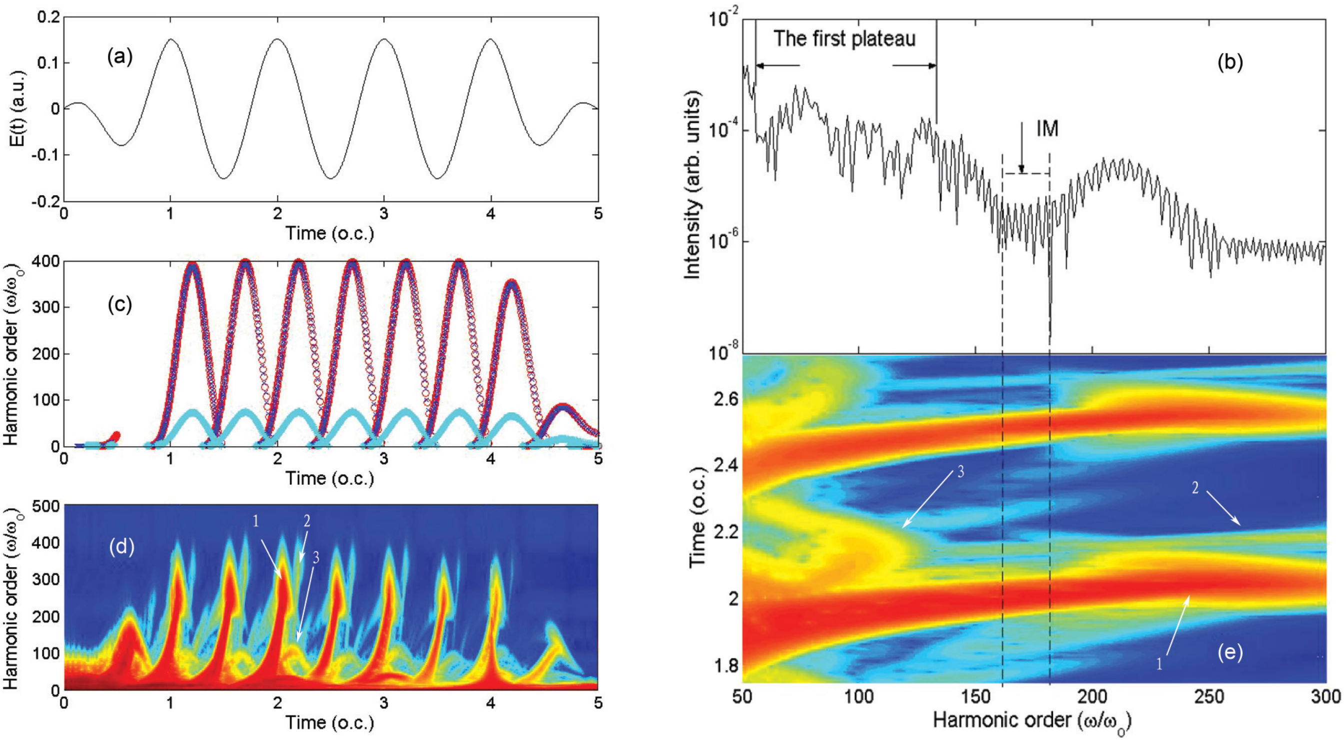

FIG. 3. (Color online) (a) Sketch of the driving electric field with a peak intensity of 8.0×10^{14} W/cm^2 and a wavelength of 1600 nm. (b) The HHG spectra from the HeH^{2+} driven by the trapezoidal pulse. (c) The classical calculation result of the emitted energy of the electron returning to the ion as a function of time. (d) The time-frequency distributions of the HHG power spectrum. (e) The enlargement of the time profile for the time from 1.75 o.c. to 2.75 o.c.

larger than that of He→e→H process. On the other hand, some of the electrons may accelerate directly to H$^+$ from He atom. When the laser field reverses its direction, the electron may return back to He^{2+} and recombine with He^{2+} (He→H→He). Due to the lack of accelerating in the laser field, the maximal kinetic energy the returning electron can acquire is lower than the two cases mentioned above; thus the energy emitted from (He→H→He) process contributes to the low-order region of the harmonics. In addition, for HeH^{2+} molecular ion, the electron is mainly localized on the He^{2+}; hence the electron ionized from the H$^+$ (H→e→He, H→e→H) can be ignored. In a word, there are three major channels of recombination in molecular HHG for HeH^{2+} molecular ion, marked as 1, 2, and 3 in Fig. 2. The first (He→e→He) and the second (He→e→H) channels contribute to the high-order region of the harmonics, but the intensity of the second one is very low; the third one (He→H→He) emits a lower-harmonic photon.

Based on the above analysis, the multichannel interference in the process of molecular HHG for the HeH^{2+} molecular ion is investigated. The monochromatic trapezoidal laser field (1600 nm, 8.0×10^{14} W/cm^2) shown in Fig. 3(a) is adopted, and the HHG spectrum driven by the laser field is presented in Fig. 3(b). At first glance, the spectrum shows the typical structure: The plateau spans a broad bandwidth and exhibits an almost constant intensity, and then drops steeply for the highest harmonics in the cutoff. However, the fine structure is quite different from that of atom and symmetric molecule. Two clear plateaus are observed before and after the 130th harmonic order, and the first plateau is irregular; by contrast, the second plateau is rather regular. Moreover, a considerable suppression, named interference minimum (IM), on the second plateau is also observed. To explain the spectrum of molecular HHG for the HeH^{2+} molecular ion, both the classical theory and quantum time-frequency analysis are adopted. Figure 3(c) shows the classical electron trajectories calculations of the HHG. It can be seen clearly that the emission times of harmonics in each laser cycle follow three characteristic electron trajectories. The first one [the blue cross in Fig. 3(c)] and the second one [the red circle in Fig. 3(c)] have almost the same maximal kinetic energy ($E_p^{\max} = 3.17U_p + I_p$) the returning electron can acquire, which matches the prediction of the semiclassical three-step model [16]. Homonuclear or heteronuclear recombination is most likely to be responsible for the two trajectories which have higher kinetic energy. In other words, the two trajectories are attributed to the He→e→He or the He→e→H process. Very different from the previous two trajectories, the third one [the cyan star in Fig. 3(c)] contributes to the low-order region of the harmonics, which matches the character of the He→H→He process mentioned above.

To gain deeper insight into the characteristic of molecular HHG, Fig. 3(d) describes the wavelet time-frequency spectrogram of HeH^{2+} molecular ion in the monochromatic trapezoidal laser pulse, which is the function of the harmonic order at the horizontal axis; the time of emission at the vertical axis; and the color scale represents the intensity of the photons. From Fig. 3(d), the information about emission times of the photons with different energies can be obtained. It is clear that there are mainly nine dominant photoenergy peaks along the time axis, which accords well with the classical electron trajectories calculations shown in Fig. 3(c). The peaks indicate the maximum emitted energy of the returning electrons, as well as their recombination times in each optical cycle emission. Furthermore, there are three kinds of recombination paths [marked as 1, 2, and 3 in Fig. 3(d)] with different recombination times and different energy of the returning electrons in each optical cycle, which shows more details about the HHG compared with the electron trajectories calculations. In addition, the interference of the three recombination paths is also observed in each optical cycle, which is responsible for the irregular modulations in the region of the first plateau.

By comparing Figs. 3(c) and 3(d), it is quite a surprising phenomenon that in the classic model, the trajectories associated to processes of He→*e*→He and He→*e*→H are matched in time, whereas in the TDSE calculation, the short paths associated to He→*e*→H processes are delayed with respect to those associated to the He→*e*→He processes. In fact, there are three important assumptions in this computational model. First, the initial conditions of velocity and position are equal to 0 at the time of ionization. Second, as the electron escapes from the nuclei, the influence of the Coulomb potential can be omitted. Third, the model is restricted to the frozen nuclei case. Considering that the ionic potential (electron-ionic core interaction) not only affects the free electron trajectory but also influences the structure of the recolliding wave packet [48]; the discrepancy between the classical model and quantum calculation can probably be ascribed to the neglect of the Coulomb potential in the classical model.

In order to give a clear image, the enlargement of the time-frequency spectrogram for the time from 1.75 to 2.75 o.c. is presented in Fig. 3(e). It can be seen that two peaks contribute to the high-order region of the harmonic in each optical cycle. The bright peak (marked as 1) plays a dominant role in the process of HHG, implying that this peak originates from the (He→e→He) process; while the weak one (marked as 2) contributes slightly to the HHG, meaning that the peak comes from the (He→e→H) process. Additionally, it is clear that there still exists a peak with a maximum harmonic order, about 130th, originating from the (He→H→He) process, which mainly contributes to the low-order region of the harmonic. But for the first two processes, it is important to note that the long trajectories are absent in Fig. 3(d); only the short trajectories contribute to the high-order region of the harmonic. Moreover, a considerable suppression [marked by the dashed line in Fig. 3(e)] from 160th to 180th order is also found clearly, which is in good accordance with the area of the interference minimum in the harmonic spectrum shown in Fig. 3(b). Can the considerable suppression of harmonic emission be attributed to the destructive interference of different recombination paths, or the lack of the long trajectories? In the following work, we investigate the mechanism of the minimum not only by adjusting the initial vibrational state, but also by investigating the effect of the isotopic variant.

B. The effect of initial vibration state on molecular HHG process

From the discussion mentioned above, the mechanism of molecular HHG for HeH^{2+} molecular ion is explored. To further study the influence of nuclear signature on molecular HHG, the effect of the initial vibration state on molecular HHG is discussed in the following work.

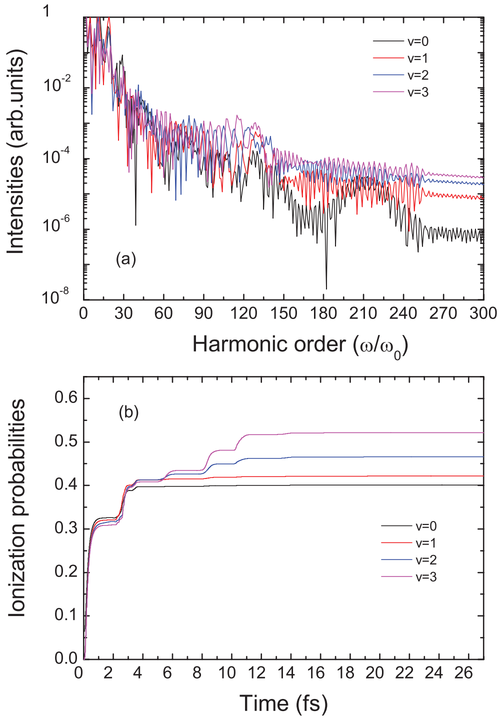

FIG. 4. (Color online) (a) HHG spectra from the different initial vibrational states of the HeH^{2+} ion ($\upsilon = 0$, 1, 2, and 3). (b) The ionization probabilities for the above four cases.

The HHG spectra driven by the monochromatic trapezoidal laser field adopted above for HeH^{2+} are shown in Fig. 4(a) for the conditions of different initial vibrational states ($\upsilon = 0$, 1, 2, and 3). Clearly, the HHG spectra share the following common features: They rapidly decay for the first few order harmonics, then this is followed by the first plateau with much more modulations, and they finally cut off through the second plateau. Furthermore, it can also be found that the destructive interference is clear in the second plateau. However, there are some distinct differences displayed in the HHG spectra. With the enhancement of the initial vibrational state, the intensities of the harmonic spectra are also enhanced, especially for the high harmonic energies, while the destructive interference becomes weaker. As we all know, the harmonic yields are sensitive to the ionization probability. Thus, to explain this enhancement of the harmonic spectra, the corresponding ionization probabilities are presented in Fig. 4(b) for the cases of $\upsilon = 0$, 1, 2, and 3. Clearly, due to the reducing of the ionization potentials for the high vibrational states, the ionization probability is reinforced with the enhancement of the initial vibrational state, which is the vital reason of the enhancement of the harmonic yields. To explain the vibration dependence of the minimum visually, the time-frequency distributions of molecular HHG spectra from 130 to 200 orders for the different vibrational states are shown in Fig. 5. It is obvious that the long trajectories are absent for different initial vibrational states. However, from Fig. 4(a) we can see that the

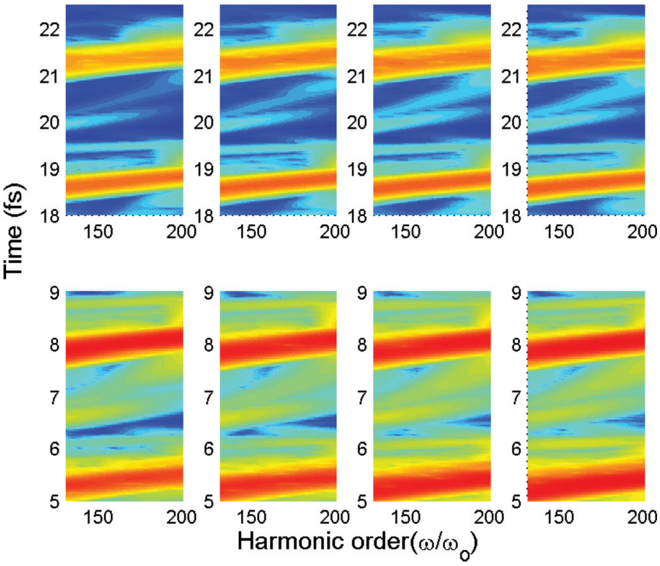

FIG. 5. (Color online) The time-frequency distributions of the HHG power spectra from 130th–200th for the different initial vibrational states of the HeH^{2+} ion ($v = 0$, 1, 2, and 3).

minimum becomes weaker by increasing the initial vibrational state, which demonstrates that the lack of the long trajectories is not the main reason for the occurrence of the minimum. Furthermore, with the enhancement of the initial vibrational state, the harmonic yield of the He→e→H process is enhanced signally while the harmonic yield of the He→e→He process is unchanged, which results in the decrease of the minimum. Consequently, the minimum is associated with interference of different processes, rather than the lack of the long trajectories.

For further understanding the harmonic enhancement mentioned above, the temporal evolution of the coupled electron-nuclear wave-packet density distribution for different initial vibrational states ($v = 0$–3) is also calculated. The first column [Figs. 6(a)–6(d)] depicts the coupled electron-nuclear wave-packet density distributions for $v = 0$ state at four different moments: (a) $t = 0$ o.c., (b) $t = 1.5$ o.c., (c) $t = 3$ o.c., and (d) $t = 4.5$ o.c. Obviously, for $v = 0$, the wave packet is located in a narrow region along the horizontal axis during the first three optical cycles [see Figs. 6(a) and 6(b)], since the driving field is just established from zero to the maximum. As a result, the wave packet cannot immediately spread and almost remains in a narrow region along the horizontal axis. While for the distribution along the vertical axis, the wave packet obviously spreads and broadens as the laser field potential is larger than the Coulomb potential. With the driving field established, the molecular system interacts with a high enough electric field for several optical cycles so that the electron-nuclear wave packet spreads and broadens [see Figs. 6(c) and 6(d)]. Moreover, with the enhancement of the initial vibrational state, the initial wave packet distributes more widely from 3.5 a.u.$<R<$4.5 a.u. at $v = 0$ to 3.0 a.u.$<R<$6.0 a.u. at $v = 3$, depicted in the first line [see Figs. 6(a), 6(e), 6(i), and 6(m)]. After the molecular system interacts with a high enough electric field, as expected, the electron-nuclear wave packet for a high-vibrational state spreads and broadens more widely than that for $v = 0$ as time proceeds, which is

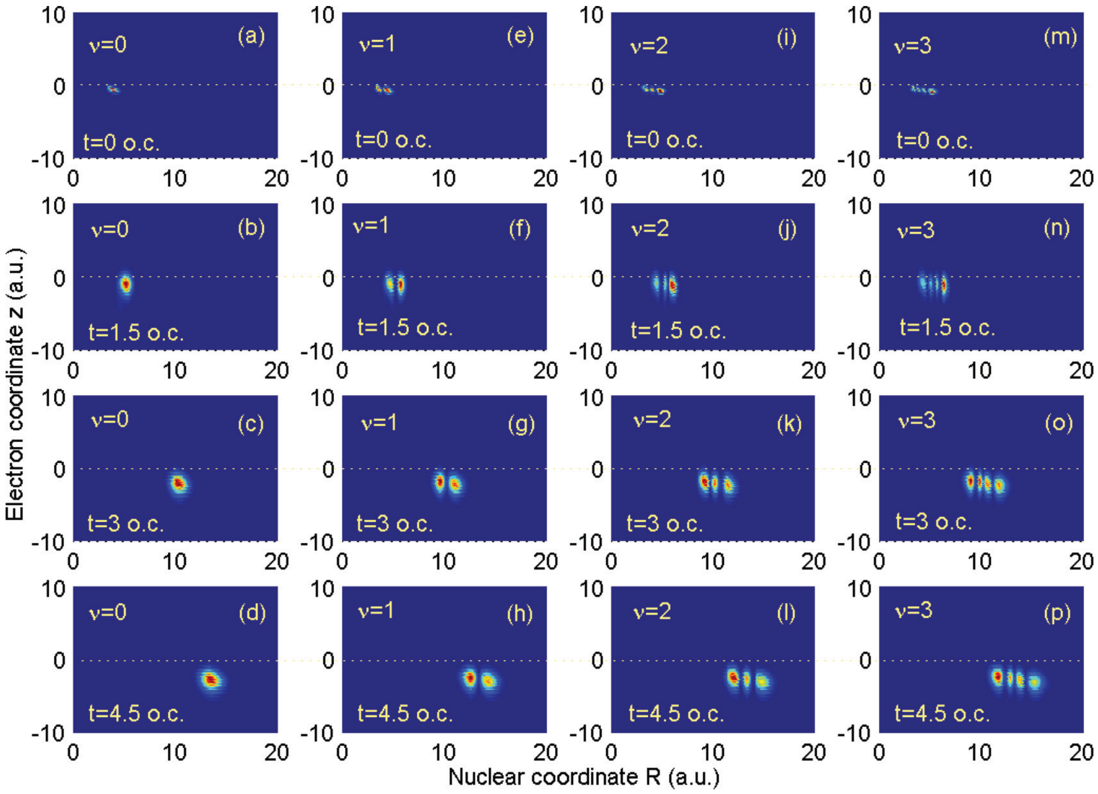

FIG. 6. (Color online) Comparison of the temporal evolution of the electron-nuclear probability density distribution of HeH^{2+} molecular ion in $2p\sigma$ electron state for $v = 0$, 1, 2, and 3 at four different evolution times from 0 to 4.5 o.c. with the time interval of 1.5 o.c.

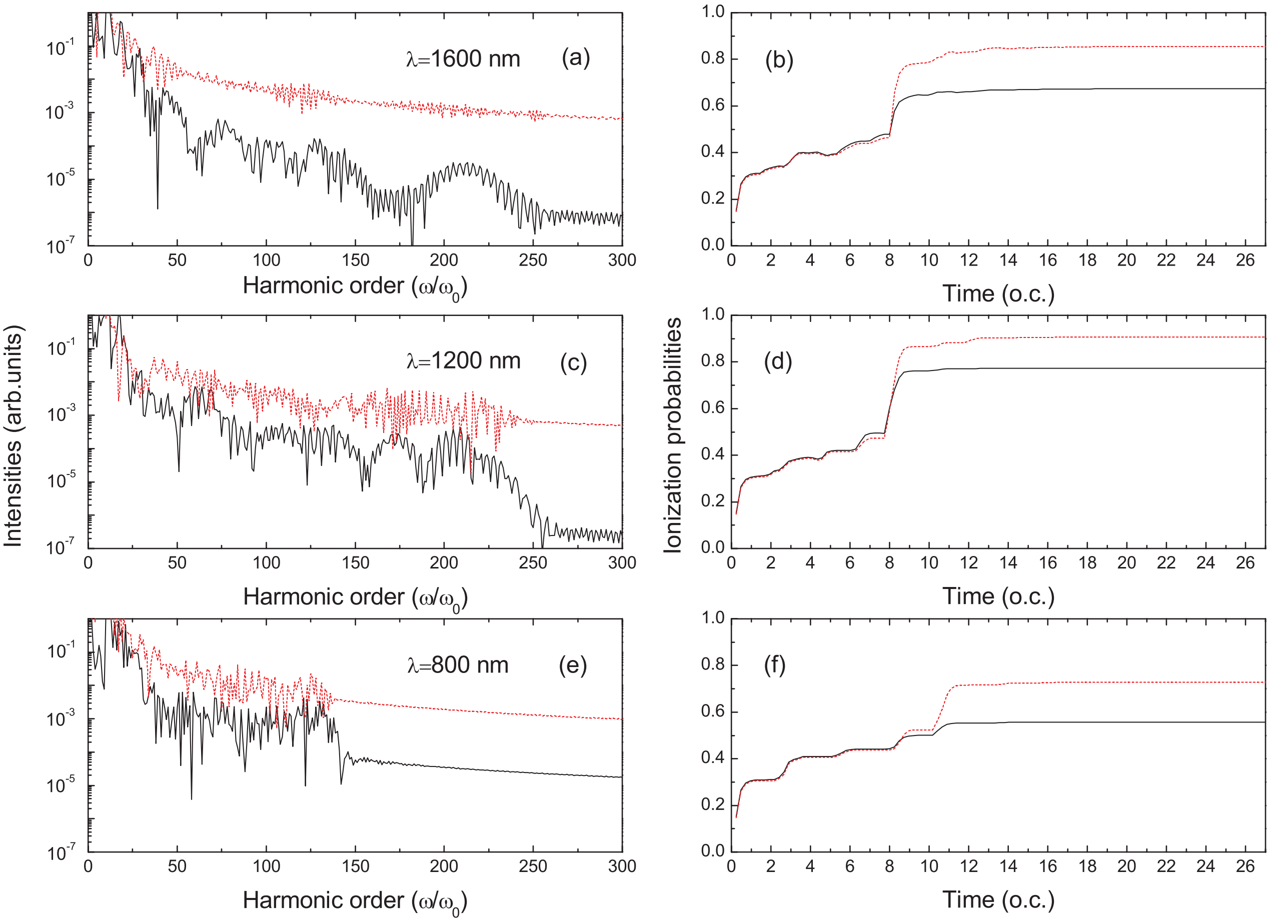

FIG. 7. (Color online) Left column: the HHG spectra from the HeH^{2+} (black solid line) and its isotopic variant HeD^{2+} (red dashed line) for different wavelengths of laser pulse. Right column: the ionization probability corresponding to different wavelengths.

the primary cause why the ionization probability is reinforced with the enhancement of the initial vibrational state.

C. The isotopic effect on molecular HHG spectra

For further capturing the nuclear signatures, the isotopic effect (HeD^{2+} ion) on the molecular HHG has also been investigated with the corresponding results shown in Fig. 7. The parameters of the laser pulse are the same as those in Fig. 3. From Fig. 7(a), it is clear that the harmonic spectrum for the HeD^{2+} ion shows the similar frequency dependence as for the HeH^{2+}, but the harmonic yields are higher for the heavy HeD^{2+} ion. To interpret this enhancement, the corresponding ionization probabilities of the HeH^{2+} and HeD^{2+} ions are presented in Fig. 7(b). Clearly, the ionization probabilities of the HeH^{2+} ion (solid black line) are lower than those of the HeD^{2+} ion (dashed red line). The present isotopic effect is similar to that in Ref. [22] for the cases of the H_2 and D_2 neutral molecules where more intense harmonics are generated in the heavier isotopes. Additionally, one can clearly see that the destructive interference in HeH^{2+} is clearer than that in HeD^{2+}. The wavelet time-frequency spectrograms of the HeH^{2+} and HeD^{2+} are shown in Figs. 8(a) and 8(b) to explain the effect of isotope on molecular HHG. From the figure, it is obvious that the shapes of the two cases are almost the same as those of Figs. 8(a) and 8(b), but the intensity of harmonic for the HeD^{2+} is much higher than that of the HeH^{2+}. It is in good accordance with the fact that the HHG spectrum of the HeD^{2+} is higher than that of the HeH^{2+}. Moreover, it is

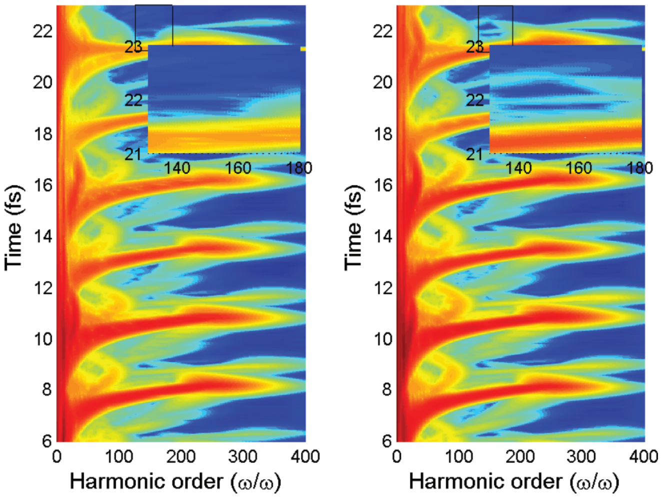

FIG. 8. (Color online) The time-frequency distributions of the HHG power spectra from the HeH^{2+} (a) and its isotopic variant HeD^{2+} (b), respectively. The insets show the enlargement of the time profile in the black solid rectangle.

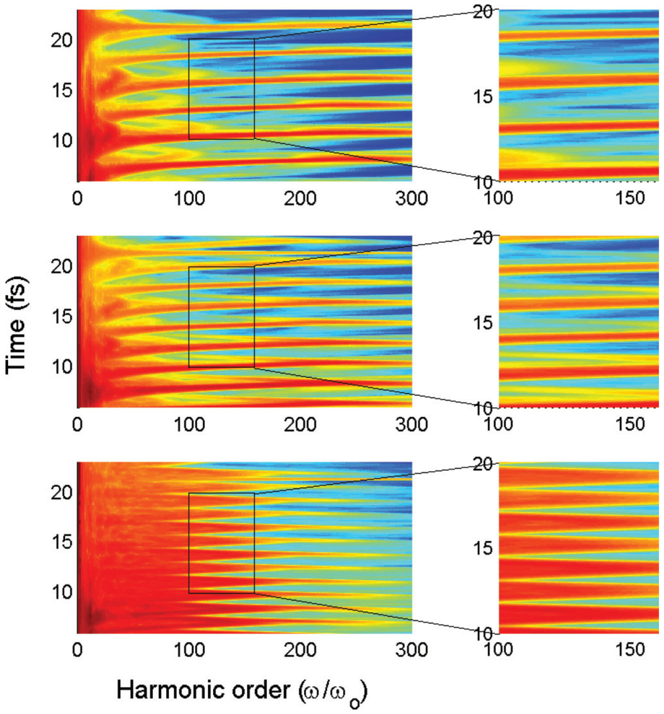

FIG. 9. (Color online) The time-frequency distributions of the HHG power spectra from the HeH^{2+} for different wavelengths of laser pulse. The insets show the detailed view of the time-frequency distributions in the black solid rectangle.

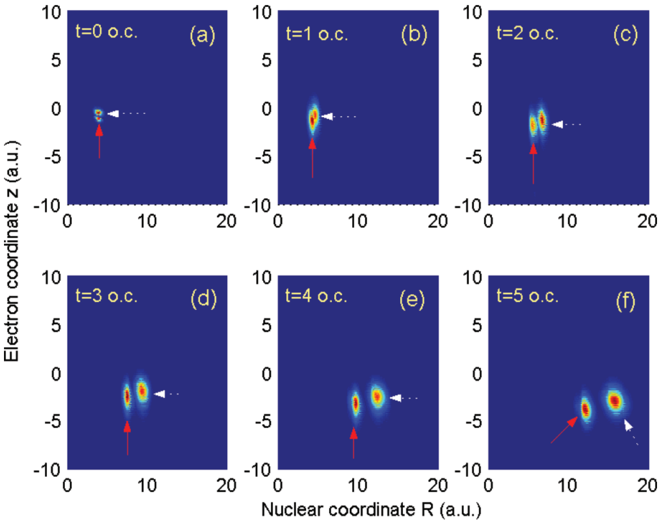

FIG. 10. (Color online) Comparison of the temporal evolutions of the nuclear-electron probability density in the $2p\sigma$ state of HeH^{2+} (marked by white dotted arrows) with HeD^{2+} (marked by red solid arrows) by a 5-o.c. trapezoidal pulse with a central wavelength of 1600 nm. Shown are snapshots of the nuclear-electron probability density distribution at (a) $t = 0$ o.c., (b) $t = 1$ o.c., (c) $t = 2$ o.c., (d) $t = 3$ o.c., (e) $t = 4$ o.c., and (f) $t = 5$ o.c.

clear that when the H of HeH^{2+} is displaced by the D, the He→e→He processes enhance a little, while the He→e→H (D) processes are enhanced signally. What is more important is that the long trajectories are all absent for the two situations. It further demonstrates that the minimum is associated with interference of different processes, rather than the lack of the long trajectories.

To further examine the influence of isotopic HeD^{2+} molecular ion, the wavelength of the laser pulse is reduced to 1200 nm [Fig. 7(c)] and 800 nm [Fig. 7(e)]. It can be seen that the harmonic yield in the heavy HeD^{2+} ion is still higher than that in the HeH^{2+}. Hence, the enhancement of the harmonic yield is mainly associated with the molecular structure rather than the parameter of laser pulse. Additionally, with the reduction of the wavelength of the laser pulse, the destructive interference becomes obscure. Figure 9 shows the time-frequency spectrograms under the driving wavelengths of 1600, 1200, and 800 nm. By decreasing the wavelength of the laser pulse, the harmonic yield of the He→e→He process is increased, while the harmonic yield of the He→e→H process is prominently suppressed. When the wavelength of the laser pulse is reduced to 800 nm, only the He→e→He process contributes to the harmonics with the complete suppression of the He→e→H process. As a result, the minimum in the second plateau disappears.

To explain the enhancement phenomena described above visually, the electron-nuclear probability density distributions at different times for HeH^{2+} (marked by the white dotted arrows) and HeD^{2+} (marked by the red solid arrows) are displayed in Fig. 10. Like the spread of the initial nuclear wave packet for HeH^{2+}, the initial wave packet for HeD^{2+} is located in a narrow region, and then it propagates to larger internuclear distance after the interaction with the laser pulse. However, there are some distinct differences. After the driving field has been established, the spread of the electron-nuclear wave packet for HeD^{2+} is slower than that for HeH^{2+} along the horizontal axis, because with smaller reduced mass, the HeH^{2+} ion experiences a stronger acceleration which leads to the faster nuclear motion. From Figs. 10(a)–10(f), compared with the case of the HeH^{2+}, it is obvious that the spread of electron-nuclear wave packet for HeD^{2+} is faster along the electron coordinate z. This can mainly account for the higher ionization and the higher harmonic intensity from the heavier HeD^{2+} ion. As a result, harmonic yield is sensitive to the molecular structure.

IV. CONCLUSIONS

In this paper, exact non-Born-Oppenheimer simulations are performed to investigate the HHG of asymmetric diatomic molecules by numerically solving the one-dimensional time-dependent Schrödinger equation. The results show that a considerable suppression in the high-order region can be observed from the harmonic spectra with two-plateau structure. By means of the classical returning kinetic energy map and the time-frequency distribution, the mechanism of molecular HHG for asymmetric molecular ion of HeH^{2+} is discussed in detail. Additionally, when HeH^{2+} molecule ions are prepared in the high-vibrational state, the nuclei vibrate violently and the emission efficiency of the HHG is enhanced. Moreover, through the investigation of the isotopic effect, it is found that more intense harmonics are generated in the heavier nucleus. Besides, the electron-nuclear probability density distributions are presented to better understand the enhancement of the asymmetric molecular HHG, from which the electron-nuclear dynamics can be revealed.

ACKNOWLEDGMENTS

The authors sincerely thank Prof. Keli Han and Dr. Ruifeng Lu for providing us the LZH-DICP code. This work is supported by the Special Funds of the National Natural Science Foundation of China (Grant No. 11047191), Key Project of Chinese Ministry of Education (Grant No. 211025), Research Fund for the Doctoral Program of Higher Education of China (Grant No. 20111404120004) and the Natural Science Foundation for Young Scientists of Shanxi Province, China (Grant No. 2009021005).

---

[1] T. Brabec and F. Krausz, Rev. Mod. Phys. **72**, 545 (2000).
[2] F. Krausz and M. Ivanov, Rev. Mod. Phys. **81**, 163 (2009).
[3] Z. Chang and P. Corkum, J. Opt. Soc. Am. B **27**, B9 (2010).
[4] A. Giusti-Suzor and F. H. Mies, Phys. Rev. Lett. **68**, 3869 (1992).
[5] E. E. Aubanel, J. M. Gauthier, and A. D. Bandrauk, Phys. Rev. A **48**, 2145 (1993).
[6] G. Yao and S. I. Chu, Phys. Rev. A **48**, 485 (1993).
[7] H. N. Du and X. Y. Miao, Spectrosc. Lett. **45**, 609 (2012).
[8] H. N. Du and X. Y. Miao, Spectrosc. Lett. **45**, 556 (2012).
[9] A. Datta, S. Saha, and S. S. Bhattacharyya, J. Phys. B **30**, 5737 (1997).
[10] B. D. Esry, A. M. Sayler, P. Q. Wang, K. D. Carnes, and I. Ben-Itzhak, Phys. Rev. Lett. **97**, 013003 (2006).
[11] B. D. Esry and I. Ben-Itzhak, Phys. Rev. A **82**, 043409 (2010).
[12] R. Kienberger, E. Goulielmakis, M. Uiberacker, A. Baltuska, V. Yakovlev, F. Bammer, A. Scrinzi, Th. Westerwalbesloh, U. Kleineberg, U. Heinzmann, M. Drescher, and F. Krausz, Nature (London, UK) **427**, 817 (2004).
[13] R. López-Martens, K. Varjú, P. Johnsson, J. Mauritsson, Y. Mairesse, P. Salières, M. B. Gaarde, K. J. Schafer, A. Persson, S. Svanberg, C.-G. Wahlström, and A. L'Huillier, Phys. Rev. Lett. **94**, 033001 (2005).
[14] C. Altucci, R. Bruzzese, C. de Lisio, M. Nisoli, E. Priori, S. Stagira, M. Pascolini, L. Poletto, P. Villoresi, V. Tosa, and K. Midorikawa, Phys. Rev. A **68**, 033806 (2003).
[15] D. S. Kim, J. J. Park, K. H. Lee, J. Park, and C. H. Nam, Jpn. J. Appl. Phys. **48**, 026506 (2009).
[16] H. Soifer, P. Botheron, D. Shafir, A. Diner, O. Raz, B. D. Bruner, Y. Mairesse, B. Pons, and N. Dudovich, Phys. Rev. Lett. **105**, 143904 (2010).
[17] D. C. Yost, T. R. Schibli, J. Ye, J. L. Tate, J. Hostetter, M. B. Gaarde, and K. J. Schafer, Nat. Phys. **5**, 815 (2009).
[18] P. B. Corkum, Phys. Rev. Lett. **71**, 1994 (1993).
[19] A. D. Bandrauk, S. Chelkowski, and S. Goudreau, J. Mod. Opt. **52**, 411 (2005).
[20] T. Zuo, S. Chelkowski, and A. D. Bandrauk, Phys. Rev. A **48**, 3837 (1993).
[21] P. Moreno, L. Plaja, and L. Roso, Phys. Rev. A **55**, R1593 (1997).
[22] M. Lein, Phys. Rev. Lett. **94**, 053004 (2005).
[23] S. Baker, J. S. Robinson, C. A. Haworth, H. Teng, R. A. Smith, C. C. Chirilă, M. Lein, J. W. G. Tisch, and J. P. Marangos, Science **312**, 424 (2006).
[24] Y. H. Guo, H. X. He, J. Y. Liu, and G. Z. He, J. Mol. Struct.: THEOCHEM **947**, 119 (2010).
[25] L. Q. Feng, and T. S. Chu, J. Chem. Phys. **136**, 054102 (2012).
[26] Q. Li, W. Hong, Q. Zhang, S. Wang, and P. Lu, Phys. Rev. A **81**, 053846 (2010).
[27] G. L. Kamta and A. D. Bandrauk, Phys. Rev. Lett. **94**, 203003 (2005).
[28] Q. Liao, P. Lu, Q. Zhang, Z. Yang, and X. Wang, Opt. Express **16**, 17070 (2008).
[29] I. Dumitriu and A. Saenz, J. Phys. B **42**, 165101 (2009).
[30] I. Ben-Itzhak, I. Gertner, O. Heber, and B. Rosner, Phys. Rev. Lett. **71**, 1347 (1993).
[31] P. F. Lan, P. X. Lu, F. Li, Q. G. Li, W. Y. Hong, Q. B. Zhang, Z. Y. Yang, and X. B. Wang, Opt. Express **16**, 17542 (2008).
[32] X.-B. Bian and A. D. Bandrauk, Phys. Rev. Lett. **105**, 093903 (2010).
[33] X.-B. Bian and A. D. Bandrauk, Phys. Rev. A **83**, 023414 (2011).
[34] X.-B. Bian and A. D. Bandrauk, Phys. Rev. A **83**, 041403(R) (2011).
[35] Y. Chen and B. Zhang, Phys. Rev. A **86**, 023415 (2012).
[36] A. D. Bandrauk, S. Chelkowski, S. Kawai, and H. Lu, Phys. Rev. Lett. **101**, 153901 (2008).
[37] A. D. Bandrauk, S. Chelkowski, and H. Z. Lu, J. Phys. B **42**, 075602 (2009).
[38] K. C. Kulander, F. H. Mies, and K. J. Schafer, Phys. Rev. A **53**, 2562 (1996).
[39] H. X. He, R. F. Lu, P. Y. Zhang, Y. H. Guo, K. L. Han, and G. Z. He, Phys. Rev. A **84**, 033418 (2011).
[40] R. F. Lu, P. Y. Zhang, and K. L. Han, Phys. Rev. E **77**, 066701 (2008).
[41] J. A. Fleck, J. R. Morris, and M. D. Feit, Appl. Phys. A **10**, 129 (1976).
[42] K. Burnett, V. C. Reed, J. Cooper, and P. L. Knight, Phys. Rev. A **45**, 3347 (1992).
[43] X. M. Tong and Sh. I. Chu, Phys. Rev. A **61**, 021802(R) (2000).
[44] X. Chu and Sh. I. Chu, Phys. Rev. A **64**, 021403(R) (2001).
[45] A. S. Alnaser, B. Ulrich, X. M. Tong, I. V. Litvinyuk, C. M. Maharjan, P. Ranitovic, T. Osipov, R. Ali, S. Ghimire, Z. Chang, C. D. Lin, and C. L. Cocke, Phys. Rev. A **72**, 030702 (2005).
[46] S. Saugout, C. Cornaggia, A. Suzor-Weiner, and E. Charron, Phys. Rev. Lett. **98**, 253003 (2007).
[47] C. Liu, Z. Zeng, P. Wei, P. Liu, R. Li, and Z. Xu, Phys. Rev. A **81**, 033426 (2010).
[48] D. Shafir, B. Fabre, J. Higuet, H. Soifer, M. Dagan, D. Descamps, E. Mével, S. Petit, H. J. Wörner, B. Pons, N. Dudovich, and Y. Mairesse, Phys. Rev. Lett. **108**, 203001 (2012).